



Focal, remote-controlled, chronic chemical modulation of brain microstructures

Khalil B. Ramadi^{a,b}, Canan Dagdeviren^c, Kevin C. Spencer^{a,d}, Pauline Joe^a, Max Cotler^{a,b}, Erin Rousseau^{a,b}, Carlos Nunez-Lopez^{a,c}, Ann M. Graybiel^{e,f}, Robert Langer^{a,b,g,1}, and Michael J. Cima^{a,b,d,1}

^aKoch Institute for Integrative Cancer Research, Massachusetts Institute of Technology, Cambridge, MA 02139; ^bHarvard–Massachusetts Institute of Technology Health Sciences and Technology Division, Massachusetts Institute of Technology, Cambridge, MA 02139; ^cMedia Lab, Massachusetts Institute of Technology, Cambridge, MA 02139; ^dDepartment of Materials Science, Massachusetts Institute of Technology, Cambridge, MA 02139; ^eMcGovern Institute for Brain Research, Massachusetts Institute of Technology, Cambridge, MA 02139; ^fDepartment of Brain and Cognitive Sciences, Massachusetts Institute of Technology, Cambridge, MA 02139; and ^gDepartment of Chemical Engineering, Massachusetts Institute of Technology, Cambridge, MA 02139

Edited by John A. Rogers, Northwestern University, Evanston, IL, and approved June 4, 2018 (received for review March 28, 2018)

Direct delivery of fluid to brain parenchyma is critical in both research and clinical settings. This is usually accomplished through acutely inserted cannulas. This technique, however, results in backflow and significant dispersion away from the infusion site, offering little spatial or temporal control in delivering fluid. We present an implantable, MRI-compatible, remotely controlled drug delivery system for minimally invasive interfacing with brain microstructures in freely moving animals. We show that infusions through acutely inserted needles target a region more than twofold larger than that of identical infusions through chronically implanted probes due to reflux and backflow. We characterize the dynamics of in vivo infusions using positron emission tomography techniques. Volumes as small as 167 nL of copper-64 and fludeoxyglucose labeled agents are quantified. We further demonstrate the importance of precise drug volume dosing to neural structures to elicit behavioral effects reliably. Selective modulation of the substantia nigra, a critical node in basal ganglia circuitry, via muscimol infusion induces behavioral changes in a volume-dependent manner, even when the total dose remains constant. Chronic device viability is confirmed up to 1-y implantation in rats. This technology could potentially enable precise investigation of neurological disease pathology in preclinical models, and more efficacious treatment in human patients.

brain | drug delivery | substantia nigra | neural implant | PET

Reliable delivery of therapeutics to specific brain structures presents a major limitation in the treatment of neurological and neuropsychiatric disorders. Failure of drug trials for these disorders has been attributed to inadequate drug distribution within brain structures (1). Drug targets implicated in such disorders have been found in many regions of the central nervous system, but in any individual case, the causative pathology may be localized to a single region of the brain. Thus, broad drug biodistribution can lead to significant off-target effects and potential toxicity at therapeutic doses (2). Focal delivery of drug could decrease adverse effects while improving treatment efficacy. Current chronic focal delivery techniques are limited to passive mechanisms with devices such as Omayya reservoirs and Gliadel wafers (3). Acute delivery is achieved with intraventricular infusions through acutely implanted needles (4). No actively controlled chronic drug delivery system for the brain is currently in clinical use. The use of optogenetics, designer receptors exclusively activated by designer drugs, and other revolutionary tools has begun to address the great heterogeneity of cells and function in neural microstructures (~1 mm³) (5–7). Even these techniques, however, rely on acute needle injections into the brain. New tools and therapies can be potentially created with the strategy of targeting specific neural structures with fine spatiotemporal resolution. Precise chemical dosing with microinvasive devices should enable such targeting of specific populations of cells based on their anatomical location (8).

Mid- and deep-brain structures often contain millimeter-scale regions critical for regulation of complex emotions and behaviors

(8, 9). Structures within the anterior cingulate cortex and striatum, for example, can modulate motor activity and value-based decision-making when specifically stimulated (8, 9). A variety of chronically implanted neural probes have been developed and reported in the literature (10–14). Few of these, however, are capable of independently targeting deep structures. Current probes are either too short to penetrate deep beneath the neocortex or require a large guide tube to be placed for reliable insertion beyond ~1 cm, introducing significant trauma and obviating the benefit of a micrometer-scale probe. Clinical drug delivery in the brain has thus far been achieved mainly through convection-enhanced delivery (CED) probes (15). CED probes, however, are relatively large (1–2 mm-diameter) and designed to target large volumes, not sub-cubic-millimeter regions (16).

We developed techniques for targeted dosing of brain microstructures with fine spatiotemporal control using custom-fabricated microprobes and leveraging miniaturized neural drug delivery systems (MiNDS) originally used for modulation of individual neuronal activity in rodents and nonhuman primates (17). Key findings in the current study include the use of MiNDS to selectively dose brain microstructures and modulate behavior effects in a volume-dependent manner. We report (i) chronic viability of MiNDS probes up to 1-y postimplantation, resulting in minimal gliosis and scar formation, (ii) positron emission tomography

Significance

The brain is composed of distinct microstructures. Many neurologic and neuropsychiatric diseases arise from dysfunction of circuits of neurons and glia affecting multiple brain regions. Novel potential drug therapies are often delivered through acutely inserted cannulas in the brain. We show that such methods target a much larger region than focal chemical dosing using a class of chronically implanted microprobes. We develop techniques to quantify dynamics of deep-brain infusions and show distinct diffusion behavior of different chemicals. Our microprobes can be independently inserted and combine multiple fluidic lumens in a submillimeter footprint. Studies using implanted drug delivery systems in rodents illustrate our system's ability to remotely control behavior and the importance of volume in modulating brain regions.

Author contributions: K.B.R., C.D., A.M.G., R.L., and M.J.C. designed research; K.B.R., C.D., K.C.S., P.J., M.C., E.R., and C.N.-L. performed research; K.B.R., K.C.S., P.J., M.C., C.N.-L., and M.J.C. analyzed data; and K.B.R., C.D., A.M.G., R.L., and M.J.C. wrote the paper.

The authors declare no conflict of interest.

This article is a PNAS Direct Submission.

Published under the PNAS license.

¹To whom correspondence may be addressed. Email: rlander@mit.edu or mjcima@mit.edu.

This article contains supporting information online at www.pnas.org/lookup/suppl/doi:10.1073/pnas.1804372115/-DCSupplemental.

Published online June 25, 2018.

(PET) techniques to quantify drug microdosing kinetics, and (iii) volume-dependent behavioral modulation in freely behaving, awake rats. We demonstrate that the volume of drug infusion, rather than drug dose, leads to different pharmacodynamics with respect to neural circuit node activity. Additional findings illustrate that PET resolves bolus dynamics and diffusion profiles of various infusates in vivo with millimeter-scale resolution. We characterize distinct infusion kinetics based on pharmacodynamics as well as electrochemical characteristics of media infused such as molecular charge and size.

Results and Discussion

We first determined the volume of brain targeted by acute needle injection. Radioactive copper-64 (Cu-64) (1.67 μL) was infused into the rat substantia nigra (SN) [anterioposterior (AP) -5.0 mm, mediolateral: -2.2 mm, dorsoventral: -8.2 mm] using established acute injection protocols in the literature (18). The rat was then immediately imaged using PET (Fig. 1A). We compared the PET findings to an identical infusion (1.67 μL ; Cu-64) through a chronically implanted probe, up to 2-mo postimplantation (Fig. 1B). Acute needle infusions targeted a brain volume over twofold higher than that targeted using chronic probes (12.92 ± 2.148 mm³ vs. 4.497 ± 0.393 mm³) (Fig. 1C), as measured using PET. Infusions through chronic probes allow for deep-brain chemical dosing with significantly greater spatial specificity.

Our probe was manufactured by combining commercially available components on custom microfabricated poly(pyromellitic dianhydride-co-4,40-oxydianiline) amic acid (PI) alignment templates. Templates were fabricated using soft lithography as shown in *SI Appendix, Fig. S1*. Individual borosilicate fibers (inner diameter = 20 μm and outer diameter = 60 μm) served as microfluidic channels. Fibers were then placed within a polyimide outer shell to enhance viability and stability, and cemented to an acrylonitrile butadiene styrene hub (Fig. 1D). A custom 3D printed cap was coimplanted to protect the protruding top of the MiNDS probe.

Modular manufacturing techniques offer versatility to interchange individual components without changing the overall assembly process. A significant drawback of widespread metallic brain probes is the inability to use magnetic resonance imaging (MRI) after implantation (19). Our probe could be imaged using T2-weighted MRI without observable tissue distortion artifacts (Fig. 1E). Varying dimensions of the outer shell allows for optimization of cross-section and rigidity of the probe. A mechanically robust outer shell obviates the need of an insertion shuttle and avoids buckling during insertion. This can also be substituted for stiffer materials such as stainless steel (Fig. 1F). Three-dimensional finite-element analysis (FEA) mechanical simulations guided the optimization of probe dimensions. MRI-compatible polyimide probes experience critical buckling loads, P_{cr} of 31.2 mN. The tunable length allows targeting of any brain region in various small and large animal species. We also fabricated two stainless-steel probes with lengths of 1 cm (S-MiNDS) and 10 cm (L-MiNDS), with P_{cr} equal to 1.79 and 17.8 mN, respectively (Fig. 1G). All probes were designed to have buckling loads at least an order of magnitude above brain penetration forces (20, 21) (Fig. 1G and *SI Appendix, Fig. S2*). The number and modality of components within MiNDS can be modified as needed. We also fabricated probes containing a tungsten recording electrode together with two fluidic channels (Fig. 1F and *SI Appendix, Fig. S3*). Components were aligned in a borosilicate trilumen aligner using vacuum tweezers (*SI Appendix, Fig. S4*). Such versatility permits for implementations of this technology in multiple contexts, including one-step optogenetics and electrofluidic interfacing (22).

Imaging of submicroliter volume infusions into the brain has thus far been achieved by ex vivo autoradiography or other anatomical methods (23, 24). The inherent limitation of these techniques is the inability to image in vivo. Here, we used PET to image microliter-scale infusions with submillimeter spatial resolution in live, anesthetized animals with implanted probes (Fig. 2A). We infused 1.67 μL of (i) unbound Cu-64, (ii) PEGylated

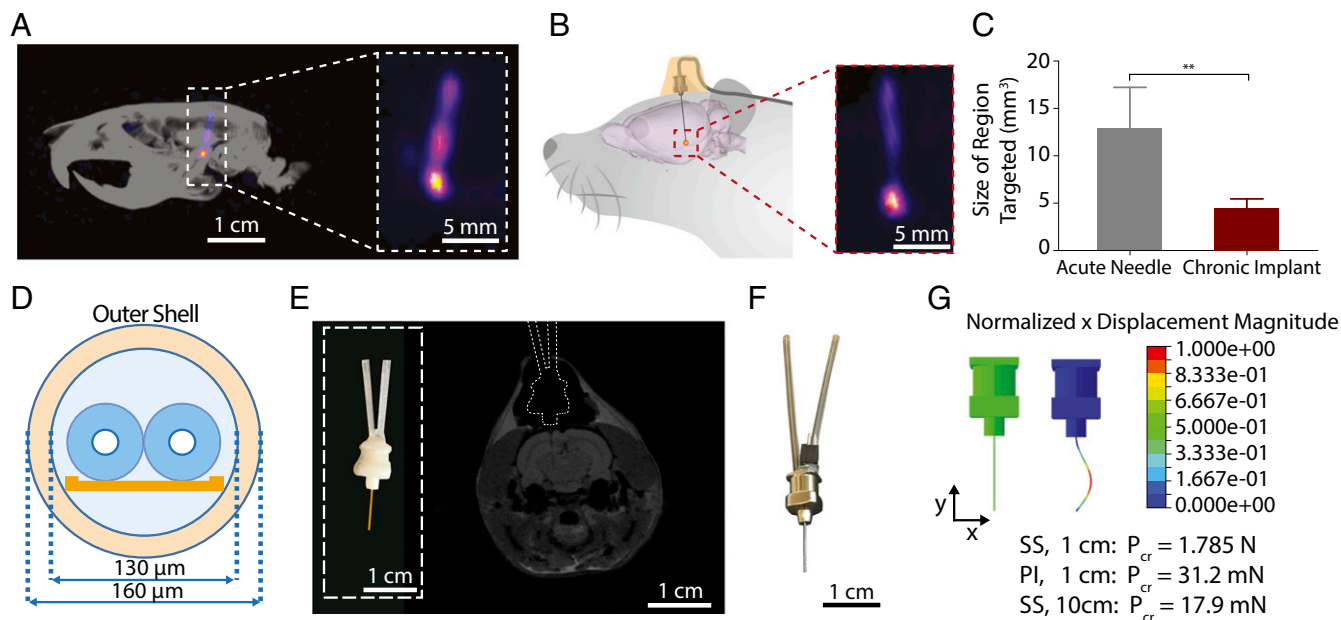


Fig. 1. Chronic MiNDS probes for focal deep-brain interfacing. (A) PET/computed tomography (PET/CT) scans of rat head following 2- μL acute injection of Cu-64 in vivo. (B) Illustration of implanted short, minimally invasive drug delivery system (S-MiNDS) probe in a rat. (Inset) PET images of 2- μL infusion of Cu-64 through chronically implanted probe. (C) Size of brain region targeted using infusion through acutely inserted needle and chronic implant. (Error bars represent SD. $**P < 0.005$, unpaired Student's *t* test.) (D) Schematic of cross-section of S-MiNDS probe showing two borosilicate fibers aligned on a polyimide (PI) template and encapsulated by an outer shell. (E) Picture of nonmetallic (PI) S-MiNDS probe and MRI image of implanted probe with overlaid probe outline. (F) Picture of stainless-steel (SS) S-MiNDS probe with two borosilicate fibers and tungsten electrode with Mill-Max pin connector. (G) FEA mechanical simulations examining critical buckling loads, P_{cr} , for PI and SS probes of various lengths. Also shown is primary buckling mode with normalized displacement magnitude.

Cu-64 (PEG-Cu-64), and (iii) 2-deoxy-2-(¹⁸F)fluoro-D-glucose (FDG) over 10 min. Imaging began simultaneously with infusion, and was conducted in 5-min intervals for 60 min. PET data were analyzed by measuring total activity included within two 3D regions of interest (ROIs). ROI 1 encompassed the region around the infusion bolus, and ROI 2 was defined as the bolus size at the point of infusion (Fig. 2 *B* and *C*). The two ROIs were volumetrically distinct and did not overlap.

Each of the three agents displayed distinct transport and diffusion kinetics. Unbound Cu-64 experienced negligible diffusion and remained localized (Fig. 2 *E-H*, *Q*, and *T* and *SI Appendix*, Fig. S5) within a 4.36-mm³ spherical bolus. Both PEG-Cu-64 and FDG, by contrast, diffused readily into the surrounding parenchyma. We modeled the decrease in activity in ROI 2 for PEG-Cu-64 and FDG as one phase exponential decay (Fig. 2*D*). PEG-Cu-64 (Fig. 2 *I-L*, *R*, and *U* and *SI Appendix*, Figs. S6 and S7) diffused with time constant of $\tau = 8.513$ min. FDG diffused more rapidly away from the infusion site ($\tau = 6.551$ min), suggesting that physical diffusion is enhanced by the relatively small

size of FDG (181 Da) compared with PEG-Cu-64 (20 kDa) (Fig. 2 *M-P*, *S*, and *V* and *SI Appendix*, Fig. S8). FDG is also manipulated by glucose transporters which could enhance clearance and transport away from the infusion site (25). PEG transport in the brain, by contrast, is dominated by passive diffusion and is unaffected by physiologic uptake or clearance processes (26). The negligible diffusion of unbound Cu-64 was likely due to intracellular influx and sequestration of copper ions by copper transporters, Ctr1, and metallothionein (27, 28). Normal copper ion trafficking processes are unable to act on Cu-64 bound to large molecules such as PEG.

The high sensitivity of PET allowed us to assess the behavior of microliter-scale infusions of different compounds in vivo. We assessed spatial distribution of nanoliter-scale volumes by infusing 167 nL of unbound Cu-64 (*SI Appendix*, Fig. S9). Infusions of, respectively, 1.67 μ L and 167 nL of Cu-64 spanned spherical volumes of 4.5 mm³ and 2.35 mm³ (*SI Appendix*, Figs. S5 and S9). Our studies illustrate that focal infusions through chronically implanted probes eliminate backflow, which is a frequent issue in

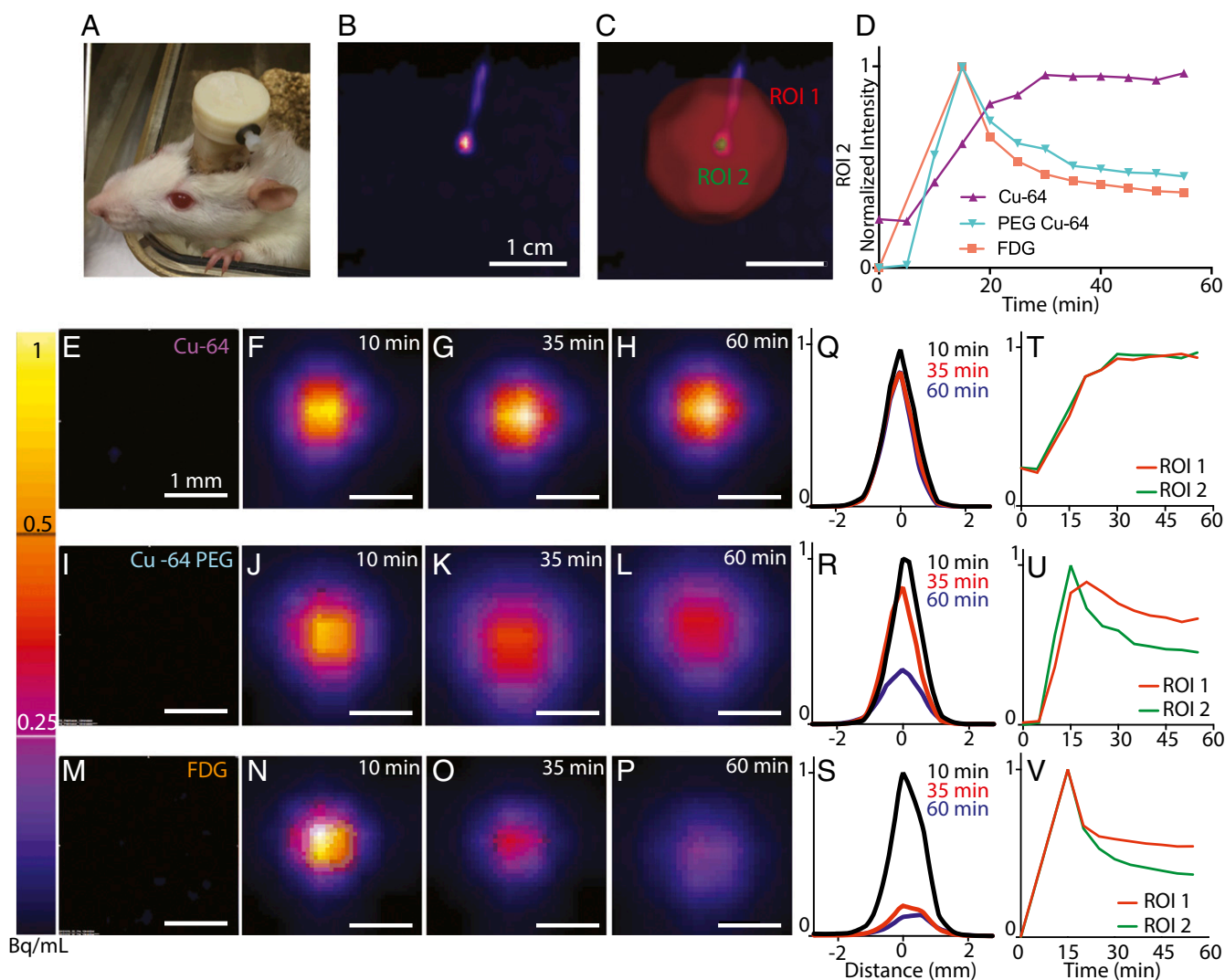


Fig. 2. PET imaging of in vivo infusions. (*A*) Picture of MiNDS probe and cap chronically implanted in a rat. (*B* and *C*) Representative 3D PET image obtained after infusion (*B*) and 3D ROI used for analysis (*C*). (*D*) ROI 2 total intensity profiles for Cu-64, PEG-Cu-64, and FDG infusions. (*E-P*) PET images of infused Cu-64 (*E-H*), PEG-Cu-64 (*I-L*), and FDG (*M-P*) bolus at $t = 0, 10, 35,$ and 60 min for 10-min infusion. (*Q-S*) Normalized intensity profile across center of bolus at $t = 10, 35,$ and 60 min after Cu-64 (*Q*), PEG-Cu-64 (*R*), and FDG (*S*) infusion onset. (*T-V*) Normalized sum intensity in ROI 1 and ROI 2 for Cu-64 (*T*, $n = 4$), PEG-Cu-64 (*U*, $n = 3$), and FDG (*V*, $n = 4$) infusions. All infusion volumes, 1.67 μ L. ROI 2 was individually computed for each trial such that the signal at the outer edge is 10% of the max signal at the center. Volume of ROI 1 was set to exactly 15 \times that of ROI 2. (Scale bars, 1 cm for *B* and *C*, 1 mm for *E-P*.)

large volume infusions. This allows for increased accuracy in targeting specific neural structures. Although MicroPET has been employed to detect large-volume (10–20 μL) CED infusions in vivo, our protocol is an instance where noninvasive in vivo imaging has been used to characterize submicroliter infusions in the brain (29, 30).

A common cause of failure of chronically implanted neural probes is that astrocytes and microglia migrate to the site of a foreign probe and mount an inflammatory response to form a glial scar (31). The scar can lead to separation of the probe from the neural tissue, disrupting function (32). In the case of deep-brain stimulation, gliotic scarring can necessitate increased voltage to maintain a therapeutic range. Astrocytes and microglia can also migrate into probes' microfluidic lumens and occlude the fluid output. Cellular-scale electrodes (5–10 μm) are increasingly prevalent as neuroscience tools, due to the low resulting gliosis (33). Analogously, we hypothesized that by minimizing the size of the MiNDS fluid outflow (20 μm), we could prevent cellular infiltration and thus avoid occlusion. We used PET to detect any increase in resistance to infusion due to gliosis and found no delay in infusion after up to 2 mo of implantation (*SI Appendix, Fig. S10A*). Impedance measurements of coimplanted tungsten electrodes demonstrated fluctuations impedance values (*SI Appendix, Fig. S10B*). Chemical microfluidic interfacing is thus as resistant to variabilities due to gliosis as electrical interfacing.

We chronically implanted MiNDS probes in rats to assess long-term device viability. Brain histological analysis was performed for 8-wk, 6-mo, and 1-y postimplantation (Fig. 3*A–E* and *SI Appendix, Fig. S11*). Immunohistochemical staining showed that the glial scar formed by astrocytes (GFAP) and microglia (Iba1) decreased with increased implantation time, down to 150 μm after 1 y postimplantation (Fig. 3*F* and *G*). Neuronal viability increased with implantation time, indicating that initial insertion trauma of the device subsided with time. Neuronal necrosis was not detected in the vicinity of the probe after 1 y of implantation (Fig. 3*H*). Implant size is a primary driver of chronic gliosis (34). Smaller probes have been reported in the literature. However, these require the use of a large guide cannula for insertion, greatly increasing trauma and subsequent gliosis, regardless of implant size. MiNDS probes are inserted independently, allowing for long-term stability and robust viability of neurons surrounding the implant.

Attenuation of local brain circuit dynamics requires precise temporal control of on/off dosing state. MiNDS probes were connected to iPrecio SMP-300 micropumps to achieve remotely controlled dosing in vivo. The fluidic functionality of MiNDS was confirmed in vitro before implantation. SMP-300 micropumps are intended for chronic low flow-rate, low-pressure infusion. The fluidic resistance of round capillaries was determined by

$$R = \frac{8\mu L}{\pi r^4}.$$

The hydraulic resistance is $1.59 \times 10^{14} \text{ kg/m}^4 \text{ s}$, equivalent to a pumping pressure of 0.44 kPa at 10 $\mu\text{L/h}$ for the shortest 1-cm capillary used. The compliant tubing of the micropump balloons during such high-pressure infusion, resulting in fluid outflow even when the pump is turned off. For a 10-min infusion at 10 $\mu\text{L/h}$ through L-MiNDS, only 5.53% of total infusion volume was delivered by 10 min (Fig. 4*A*). System compliance was minimized to avoid this problem and achieve the fine control required. Compliant styrene ethylene butylene styrene (SEBS) tubing was replaced with noncompliant flexible fluorinated ethylene propylene (FEP) tubing. An identical 10-min 10- $\mu\text{L/h}$ infusion with FEP tubing yielded 96.6% outflow of total infusion by the end of 10 min (Fig. 4*A*). FEP tubing was etched to permit bonding of medical-grade epoxy to the tubing. The connection between tubing and micropump was made by a 2-cm stainless-steel connector to reduce the effect of remaining compliant SEBS tubing within the pump peristaltic mechanism. In vitro testing of this setup confirmed that MiNDS infused reliably and consistently at flow rates across multiple orders of magnitude (0.1, 1, and 10 $\mu\text{L/h}$). The system performed with less than 7.5% or 15% overflow after end infusion across all flow rates through S-MiNDS and L-MiNDS, respectively. The smallest infused volume was 33 nL (*SI Appendix, Fig. S12*). No significant outflow was detected when the system was off, indicating negligible leakage due to passive diffusion.

We implanted MiNDS to characterize the effect of volume infused on behavioral modulation in an acute, reversible hemiparkinsonian rat model (35). This model utilizes unilateral infusion of muscimol, a GABA agonist, to the SN to elicit increased contralateral turning. Activation of inhibitory GABA circuits leads to an imbalance in motor drive on the two sides of the brain, producing circling behavior. We quantified the effect of infusion volume, rather than molecular dose, on behavior. Three volumes of

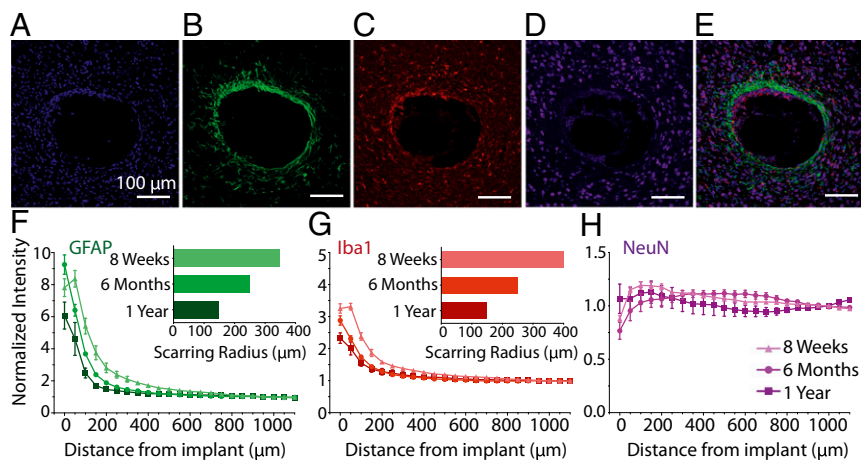


Fig. 3. Chronic implantation of probe causes minimal gliosis. (*A–E*) Confocal microscopy images of immunohistochemical staining 8-wk postimplantation of probe, showing DAPI (*A*), GFAP (*B*), Iba1 (*C*), NeuN (*D*), and merged stains (*E*). (*F–H*) Stain intensity as a function of distance from edge of implant 8-wk, 6-mo, and 1-y postimplantation for GFAP (*F*), Iba1 (*G*), and NeuN (*H*). Also shown is significant scar radius for GFAP (*F*, *Inset*) and Iba1 (*G*, *Inset*) (Error bars represent SE, significance calculated using one-way ANOVA with Dunnett correction). (Scale bars: 100 μm .)

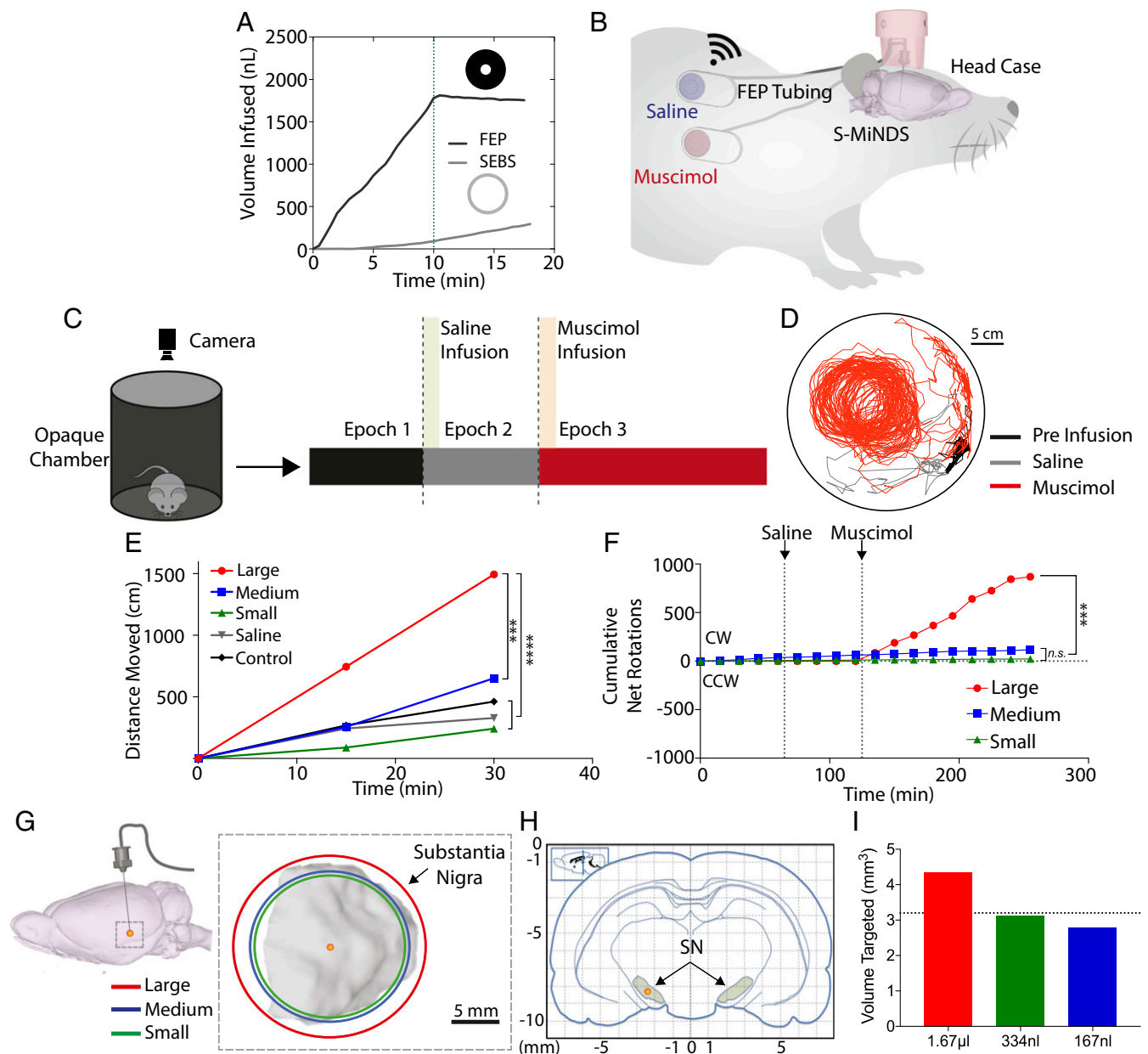


Fig. 4. Volume-dependent behavioral modulation using chronically implanted probe. (A) S-MiNDS in vitro 10-min infusion profiles using SEBS and FEP tubing. (B) Illustration of implanted MiNDS with two pumps containing saline and muscimol. (C) Experimental procedure for behavior modulation experiments. Rats implanted with MiNDS are placed in an opaque chamber, allowed to acclimate, and imaged for 4 h during periods of preinfusion (epoch 1), after saline infusion (epoch 2), and after consequent muscimol infusion (epoch 3). Rats received small (167 nL), medium (334 nL), or large (1.67 μL) volume infusions of both saline and muscimol. (D) Sample movement trace of a rat in chamber over all three epochs. (E) Distance moved during first 30 min of epoch 3. (** $P < 0.0002$, **** $P < 0.0001$, two-way ANOVA with Tukey correction.) (F) Net cumulative clockwise (CW) minus counterclockwise (CCW) rotations over time (*n.s.*, not significant). (G) Schematic of rat brain and SN, illustrating region dosed by each volume infusion, as calculated using PET images. (H) Coronal section of rat brain (AP = -5.02 mm from bregma) showing shaded SN on both sides and infusion site on left side (red dot). (I) Size of brain region targeted by small (167 nL, eight trials), medium (334 nL, eight trials), or large (1.67 μL, nine trials) volume infusions, compared with volume of SN (3.2 mm³; dashed line).

muscimol (1.67 μL, 334 nL, or 167 nL) were infused into the SN while maintaining an identical dose (total dose = 334 ng).

Each microfluidic fiber in an MiNDS probe was connected to a wireless micropump (iPrecio SMP-300). Rats were implanted with MiNDS and two pumps (Fig. 4B). Each of the pumps implanted was filled with muscimol or saline. Each trial consisted of three epochs. (i) Rats were first placed in an imaging chamber and imaged to record baseline behavior. (ii) Saline was then infused over 10 min (1.67 μL, 334 nL, or 167 nL). (iii) Fifty minutes later, the other pump infused an equal volume of muscimol over

10 min. The animals were imaged for 2 h after muscimol infusion (Fig. 4C). Behavior in each epoch was analyzed using Ethovision software (Noldus) to calculate the total distance moved as well as clockwise and counterclockwise rotations (Fig. 4D). The 167-nL muscimol infusion had no discernible effect on behavior (*SI Appendix, Figs. S13 and S14*). Rats receiving medium volume (334 nL) muscimol infusions displayed a twofold increase in activity and increased rotational preference to the contralateral side (*SI Appendix, Figs. S15 and S16*). No significant difference in either distance moved or cumulative rotations was found between animals

receiving small and medium volumes. Large volume (1.67- μ L) muscimol infusions had a significant and repeatable effect on behavior. These rats exhibited a sixfold increase in distance traveled over 30 min and 40-fold increase in net contralateral rotations (Fig. 4 E and F and *SI Appendix*, Figs. S17 and S18). The hemiparkinsonian effect of muscimol delivered to the SN thus is volume-dependent rather than dose-dependent. A possible explanation for the volume dependency is that GABA receptors across the SN must be stimulated for significant behavioral effects to be elicited. That is, partial inhibition leads to compensatory mechanisms by noninhibited circuitry and therefore negligible disturbance to the motor circuit and consequent behavioral effect. A review of previous studies investigating turning behavior induced by muscimol delivery to the SN reveals successful behavior modulation with volumes as small as 100 nL (*SI Appendix*, Fig. S19). These studies, however, employed acute needle injections, which likely lead to backflow and wider distribution of drug upon needle retraction (Fig. 1A). This is in contrast to the infusions through chronically implanted probes here. Cu-64 PET data illustrate that the 1.67- μ L and 167-nL infusions target spherical volumes of at least 4.5 mm³ and 2.35 mm³ (*SI Appendix*, Figs. S5 and S9). Based on this estimate, only the largest volume infusion (1.67 μ L) spans the entire 3.2-mm³ SN (36) (Fig. 4 G–I). Our findings suggest that effective inhibition of GABA within the SN is only achieved by infusing sufficient volume to span the entire SN, which was realized only by large-volume (1.67 μ L) infusions. Different molecules have different diffusivities in brain parenchyma. Our analysis of the effects of varying volumes of muscimol indicates that a high-concentration, small-volume point source is not as effective in inducing neuromodulatory responses as that of a less concentrated, larger-volume infusion.

- Nutt JG, et al.; ICV GDNF Study Group (2003) Randomized, double-blind trial of glial cell line-derived neurotrophic factor (GDNF) in PD. *Neurology* 60:69–73.
- Wolak DJ, Thorne RG (2013) Diffusion of macromolecules in the brain: Implications for drug delivery. *Mol Pharm* 10:1492–1504.
- Frosina G (2016) Advances in drug delivery to high grade gliomas. *Brain Pathol* 26: 689–700.
- Gill SS, et al. (2003) Direct brain infusion of glial cell line-derived neurotrophic factor in Parkinson disease. *Nat Med* 9:589–595.
- Deisseroth K (2015) Optogenetics: 10 years of microbial opsins in neuroscience. *Nat Neurosci* 18:1213–1225.
- Chung K, Deisseroth K (2013) CLARITY for mapping the nervous system. *Nat Methods* 10:508–513.
- Roth BL (2016) DREADDs for neuroscientists. *Neuron* 89:683–694.
- Crittenden JR, Graybiel AM (2011) Basal Ganglia disorders associated with imbalances in the striatal striosome and matrix compartments. *Front Neuroanat* 5:59.
- Amemori K, Graybiel AM (2012) Localized microstimulation of primate pregenual cingulate cortex induces negative decision-making. *Nat Neurosci* 15:776–785.
- Spieth S, et al. (2012) An intra-cerebral drug delivery system for freely moving animals. *Biomed Microdevices* 14:799–809.
- Lee HJ, et al. (2015) A new thin silicon microneedle with an embedded microchannel for deep brain drug infusion. *Sens Actuators B Chem* 209:413–422.
- Ikemoto S, Sharpe LG (2001) A head-attachable device for injecting nanoliter volumes of drug solutions into brain sites of freely moving rats. *J Neurosci Methods* 110:135–140.
- Wu F, et al. (2013) An implantable neural probe with monolithically integrated dielectric waveguide and recording electrodes for optogenetics applications. *J Neural Eng* 10:056012.
- Sohal HS, et al. (2014) The sinusoidal probe: A new approach to improve electrode longevity. *Front Neuroeng* 7:10.
- Mehta AM, Sonabend AM, Bruce JN (2017) Convection-enhanced delivery. *Neurotherapeutics* 14:358–371.
- Heiss JD, Walbridge S, Asthagiri AR, Lonser RR (2010) Image-guided convection-enhanced delivery of muscimol to the primate brain. *J Neurosurg* 112:790–795.
- Dagdeviren C, et al. (2018) Miniaturized neural system for chronic, local intracerebral drug delivery. *Sci Transl Med* 10:eaa2742.
- Zhang F, et al. (2010) Optogenetic interrogation of neural circuits: Technology for probing mammalian brain structures. *Nat Protoc* 5:439–456.
- Koch KM, et al. (2010) Magnetic resonance imaging near metal implants. *J Magn Reson Imaging* 32:773–787.
- Sharp AA, Ortega AM, Restrepo D, Curran-Everett D, Gall K (2009) In vivo penetration mechanics and mechanical properties of mouse brain tissue at micrometer scales. *IEEE Trans Biomed Eng* 56:45–53.

These results demonstrate the importance of chronic focal drug administration for chemical neural interfacing. The variability in behavioral modulation as a result of volume highlights the importance of fine-tuned local delivery to specific brain structures. Successful modulation of the nigral function only occurred with extensive, but still focal, coverage of the SN. The highly sensitive PET in vivo imaging techniques developed here are essential tools to characterize the dynamics of drug actions and microdosing in the brain. These insights are vital when conducting optogenetic and chemogenetic studies relying on discrete volume infusions of virus for transfection. Neurologic disease often arises due to a loss of normal dynamics in neural circuitry as a result of a malfunctioning node (37). Modulating the pathologic node directly allows restoration of the dynamics of the circuit (38). These collective results are important steps toward the translation of localized brain drug therapy to the clinic.

Materials and Methods

All animal studies were approved by the Committee on Animal Care, Massachusetts Institute of Technology. Materials and procedures for device fabrication and characterization can be found in *SI Appendix*, *SI Materials and Methods*. All in vivo studies and subsequent data analysis protocols are described in *SI Appendix*, *SI Materials and Methods*.

ACKNOWLEDGMENTS. We thank Preksha Bhagchandani and Cathy Choi for their technical support during device fabrication. We thank Howard Mak of the Animal Imaging Core Facility at the Koch Institute for Integrative Cancer Research for his assistance with PET imaging. We acknowledge the facilities at the Center for Nanoscale Systems at Harvard University and the Massachusetts Institute of Technology Microsystems Technology Laboratories. This work is supported by the US National Institutes of Health, National Institute of Biomedical Imaging and Bioengineering (R01 EB016101 to R.L., A.M.G., and M.J.C.) and in part by the National Cancer Institute (P30-CA14051 to the Koch Institute Core).

- Jensen W, Yoshida K, Hofmann UG (2006) In-vivo implant mechanics of flexible, silicon-based ACREO microelectrode arrays in rat cerebral cortex. *IEEE Trans Biomed Eng* 53:934–940.
- Park S, et al. (2017) One-step optogenetics with multifunctional flexible polymer fibers. *Nat Neurosci* 20:612–619.
- Martin JH (1991) Autoradiographic estimation of the extent of reversible inactivation produced by microinjection of lidocaine and muscimol in the rat. *Neurosci Lett* 127: 160–164.
- Prabhu SS, et al. (1998) Distribution of macromolecular dyes in brain using positive pressure infusion: A model for direct controlled delivery of therapeutic agents. *Surg Neurol* 50:367–375, discussion 375.
- Yu AS, et al. (2010) Functional expression of SGLTs in rat brain. *Am J Physiol Cell Physiol* 299:C1277–C1284.
- Jain A, Jain SK (2008) PEGylation: An approach for drug delivery. A review. *Crit Rev Ther Drug Carrier Syst* 25:403–447.
- Petris MJ, Smith K, Lee J, Thiele DJ (2003) Copper-stimulated endocytosis and degradation of the human copper transporter, hCtr1. *J Biol Chem* 278:9639–9646.
- Tapia L, et al. (2004) Metallothionein is crucial for safe intracellular copper storage and cell survival at normal and supra-physiological exposure levels. *Biochem J* 378: 617–624.
- Sirianni RW, Zheng MQ, Saltzman WM, Huang Y, Carson RE (2013) Direct, quantitative, and noninvasive imaging of the transport of active agents through intact brain with positron emission tomography. *Mol Imaging Biol* 15:596–605.
- Sirianni RW, et al. (2014) Radiolabeling of poly(lactic-co-glycolic acid) (PLGA) nanoparticles with biotinylated F-18 prosthetic groups and imaging of their delivery to the brain with positron emission tomography. *Bioconjug Chem* 25:2157–2165.
- De Faveri S, et al. (2014) Bio-inspired hybrid microelectrodes: A hybrid solution to improve long-term performance of chronic intracortical implants. *Front Neuroeng* 7:7.
- Butson CR, Maks CB, McIntyre CC (2006) Sources and effects of electrode impedance during deep brain stimulation. *Clin Neurophysiol* 117:447–454.
- Schwerdt HN, et al. (2017) Subcellular probes for neurochemical recording from multiple brain sites. *Lab Chip* 17:1104–1115.
- Spencer KC, et al. (2017) Characterization of mechanically matched hydrogel coatings to improve the biocompatibility of neural implants. *Sci Rep* 7:1952, and erratum (2017) 7:12812.
- Martin GE, Papp NL, Bacino CB (1978) Contralateral turning evoked by the intranigral microinjection of muscimol and other GABA agonists. *Brain Res* 155:297–312.
- Paxinos GWC (2007) *The Rat Brain in Stereotaxic Coordinates* (Academic, San Diego), 6th Ed.
- Uhlhaas PJ, Singer W (2006) Neural synchrony in brain disorders: Relevance for cognitive dysfunctions and pathophysiology. *Neuron* 52:155–168.
- Nectow AR, et al. (2017) Identification of a brainstem circuit controlling feeding. *Cell* 170:429–442.e11.